Raspberry-like hollow SnO$_2$-based nanostructures for sensing VOCs and ammonia

Wenjun Yan[1] · Xiaomin Zeng[2] · Gu Wu[2] · Wei Jiang[2] · Di Wei[2] · Min Ling[2] · Houpan Zhou[1] · Chunwei Guo[1]

Abstract

The raspberry-like hollow SnO$_2$-based (bare SnO$_2$ and Pd-doped SnO$_2$) nanostructures with different dominant crystal facets were prepared facilely using carbon nanospheres as templates via solvothermal method. Volatile organic compounds (VOCs) and ammonia (NH$_3$) gas sensing performances of the hollow SnO$_2$-based structures were studied systematically. The gas sensing performances were investigated in a temperature range of 150–315 °C. It was found that 285 °C was the optimum operating temperature for both the sensors. The SnO$_2$ sensor showed excellent VOCs (1–100 ppm) sensing performances, with a fast response/recovery behavior (around 4 s/30 s) at 285 °C. While the Pd-SnO$_2$ sensor displayed selective NH$_3$ sensing characteristics at low concentrations of 1.5–12 ppm, interestingly, with a response/recovery time of about 4 s/80 s at 285 °C. Both the SnO$_2$ and Pd-SnO$_2$ sensors showed great repeatability for 8 response/recovery cycles, and very slight response recession for a long period. It was found that not only the morphology, the synergistic effect from the heterojunctions of doped Pd and SnO$_2$, and the Pd catalysis, but also the crystal facets could modulate the sensing performance of metal oxides.

1 Introduction

Volatile organic compounds (VOCs) are important precursors of urban haze and photochemical smog. Certain VOCs are identified as hazardous gases and could cause severe diseases (e.g., lung cancer and allergy) [1]. They are encountered in various activities, such as oil refining, driving, cooking, painting, and so on. In order to evaluate the air quality, environmental monitoring is essential. Ammonia is a colorless and toxic gas with a pungent odor, and it

✉ Wenjun Yan
yanwenjun@hdu.edu.cn

✉ Houpan Zhou
houpan@hdu.edu.cn

✉ Chunwei Guo
gcw@hdu.edu.cn

[1] Smart City Research Center, School of Automation, Hangzhou Dianzi University, Hangzhou 310018, China

[2] Provincial Key Laboratory of Advanced Chemical Engineering Manufacture Technology, College of Chemical and Biological Engineering, Zhejiang University, Hangzhou 310027, China

could be noticed at a low level of 5 ppm in real environment [2]. Additionally, ammonia is immediately dangerous to life and health at a concentration of 300 ppm, causing damage to the skin, eyes, and respiratory systems of human beings [3, 4]. To ensure human safety, durable NH$_3$ sensors are indispensable.

Chemi-resistive gas sensors based on tin dioxide (SnO$_2$) has attracted widespread attention, and is considered as the most promising gas sensing material due to its low cost, high chemical durability and simple preparation [5–10]. As elucidated, response of resistive gas sensors is closely related to the amounts of active sites on the sensing material surface [11]. Various porous nanostructures (such as hollow spheres [7, 12], porous films [13, 14], et al.) have been designed to circumvent superior gas sensing performance, providing lots of surface active sites and well surface permeability. Among of them, SnO$_2$ hollow nanostructures exhibit notably interesting gas sensing performance, due to their additional exterior openings and inner voids inducing large surface area [7, 12, 15, 16].

Moreover, sensors based on undoped SnO$_2$ usually exist significant shortages, especially the lack of selectivity and low response at low analyte concentration [17, 18]. Noble metals (e.g., Pd, Ag, Pt) doping has proved to be the most suitable approach to overcome these weaknesses of pure SnO$_2$, due to the catalytic properties and the special

synergistic effects in heterojunctions between the noble metal and SnO$_2$ [17, 18]. According to the previous reports, Pd doping could improve the selective sensing of metal oxides to NH$_3$ [19, 20]. Additionally, selectively exposing facets of the sensing material has been elucidated previously to improve the gas sensing properties of metal oxides [17, 21]. In the literature [21], (221) facet with higher surface energy of SnO$_2$ could improve the sensitivity to ethanol than (110) facet with lower surface energy. Crystallographic facets effect has been extensively investigated in catalyst field, nevertheless, this effect on metal oxides sensors is still limited and quite elusive.

Herein, raspberry-like hollow SnO$_2$ and Pd-SnO$_2$ nanostructures with different dominant crystal facets are implemented facilely using carbon nanospheres as templates via solvothermal method. The VOCs and NH$_3$ sensing performances of the synthesized products are investigated, by integrating the products on micro-hotplates. Due to the special hollow structure with additional exterior openings and inner voids, different crystal facets, and the Pd doping, greatly superior VOCs sensor devices based on SnO$_2$ and NH$_3$ sensor devices based on Pd-SnO$_2$ are prepared. The corresponding sensing mechanism is proposed together with the first-principles calculation.

2 Experiments

2.1 Materials and synthesis

The carbon spheres were hydrothermally prepared according to the reported method [22]. In order to prepare SnO$_2$-based hollow structures, 3.6 g synthesized carbon spheres were dispersed into 90 mL ethanol with ultrasonic agitation, and a homogeneous supernatant solution (labeled A) was obtained. Meanwhile, 15 mmol SnCl$_2$·2H$_2$O was dispersed in 15 mL DI water to form a solution as labeled B. Solution B was added into solution A drop by drop with ultrasonic agitation. Afterwards, 0 or 0.15 mmol PdCl$_2$ was added into the mixed solution, and then kept stirring for 16 h to ensure a sufficient diffusion of Sn^{2+} onto the surface of carbon spheres because of the hydrogen bond interactions. After that, precipitates were collected by centrifugation, washed with DI water and ethanol 3 times successively, and dried at 80 °C in air. Finally, the product was calcinated in air at 500 °C for 2 h with the heating rate of 2 °C/min. The raspberry-like hollow SnO$_2$ and Pd-SnO$_2$ nanostructures were obtained.

2.2 Characterization

The morphology of the SnO$_2$ and Pd-SnO$_2$ products was characterized by the scanning electron microscopy (SEM, FEI Nanosem 430) and transmission electron microscopy

(TEM, JEOL JEM-2100). Powder X-ray diffraction (XRD) analyses were performed on a Bruker D8 Advance diffractometer with Cu Kα radiation ($\lambda \approx 1.54$ Å). X-ray photoelectron spectra (XPS) were performed on an RBD upgraded PHI-5000C ESCA system (PerkinElmer). BET surface areas were determined by (Quantachrome Inc., USA) nitrogen adsorption and desorption method.

2.3 Sensor fabrication

The gas sensor was prepared by integrating SnO$_2$-based products onto the center of a commercial aluminum oxide micro-hotplate. On the front of the micro-hotplate is interdigitated electrodes for integrated sensing material, while the back is the heating electrode for providing needed temperatures. Figure S1 shows the voltage input to the micro-hotplate versus temperature of the micro-hotplate. The SnO$_2$-based products were sonicated into suspension in an aqueous solution of isopropyl alcohol (0.5 mg/mL). A 1 µL drop was placed onto the micro-hotplate, while the micro-hotplate was heated to 100 °C and maintained there for 2 h to promote solvent evaporation and material deposition at the center of the hotplate. Figure 1a displays the schematic structure of the sensor device, with interdigitated electrodes for sensing layer resistance readout and heater circuitry for sensing temperature controlling.

2.4 Sensor testing

The gas sensing properties were investigated by a homemade measuring system with an 8 L glass test chamber as shown in Figure S2. Before measurements, the chamber is filled with ambient air. When an analyte gas was injected into the
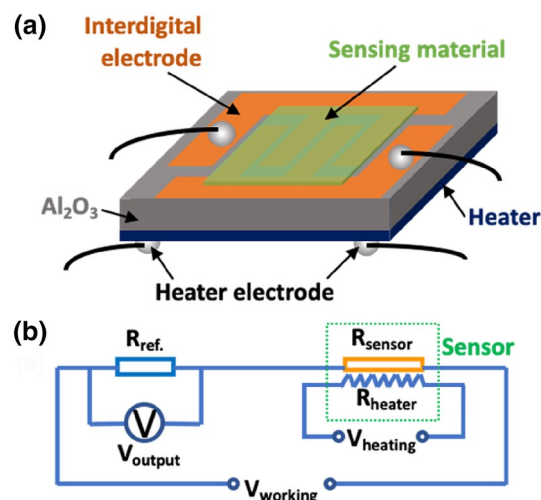

Fig. 1 **a** Schematic structure of the sensor device, **b** the working principle of the gas sensing measurement

chamber, sensor resistance began to change. Concentration of an analyte was controlled by amount of the injected pure gas. Relative humidity (RH) is adjusted by air conditioner and humidifier. Both the sensor signal collection and the micro-hotplate temperature are controlled using a Keithley 2602B source-meter. In order to form a measurement circuit, a reference resistor ($R_{ref.}$) was put in series. The circuit diagram is illustrated in Fig. 1b. By monitoring the voltage (V_{output}) across $R_{ref.}$, the sensor response (R_{sensor}) could be calculated by Ohm's law according to the Eq. (1):

$$R_{sensor} = \frac{V_{working} - V_{output}}{V_{output}} \times R_{ref} \qquad (1)$$

Response is defined by the percentile resistance change when the sensor is exposed to an analyte gas as follows:

$$Response = \frac{(R_0 - R_g)}{R_0} \times 100\% \qquad (2)$$

where R_0 and R_g are the resistances of the sensor before and after exposed to the test gas, respectively.

3 Results and discussion

3.1 Characterization

SEM image in Fig. 2a shows that carbon spheres have well-defined spherical shape and roughly 70 nm in sphere diameters. SEM image in Fig. 2b exhibits the raspberry-like hollow nanostructures of Pd-SnO$_2$ inherited from the structure of carbon spheres. During the synthesis process, the carbon spheres derived from hydrothermal conditions were hydrophilic with plenty of $-OH$ and C=O groups on the surface. These functional groups enabled the carbon spheres to bind Sn^{2+}. The carbon cores could be sacrificed in the form of CO$_2$ during calcination. Hence, the hollow structures were induced by the carbon spheres loaded with Sn^{2+} after calcination [5, 22]. The hollow structures possess small openings like raspberries, leading to great surface accessibility and effect gas diffusion and contributing to the gas sensing behavior. The Brunauer–Emmett–Teller (BET) specific area of Pd-SnO$_2$ is 25 m^2/g according to the N$_2$ adsorption–desorption measurement (shown in Fig. S3), which is slightly higher than that of the reported Pt-SnO$_2$ hollow nanospheres exhibiting extreme ethanol sensitivity [8].

The XRD patterns for SnO$_2$ and Pd-SnO$_2$ products are shown in Fig. 2c. All the peaks could be assigned to the tetragonal rutile SnO$_2$ (JCPDS No. 41-1445). The obvious characteristic peaks for SnO$_2$ at $2\theta = 26.8°$, 33.9°, 38.1° and
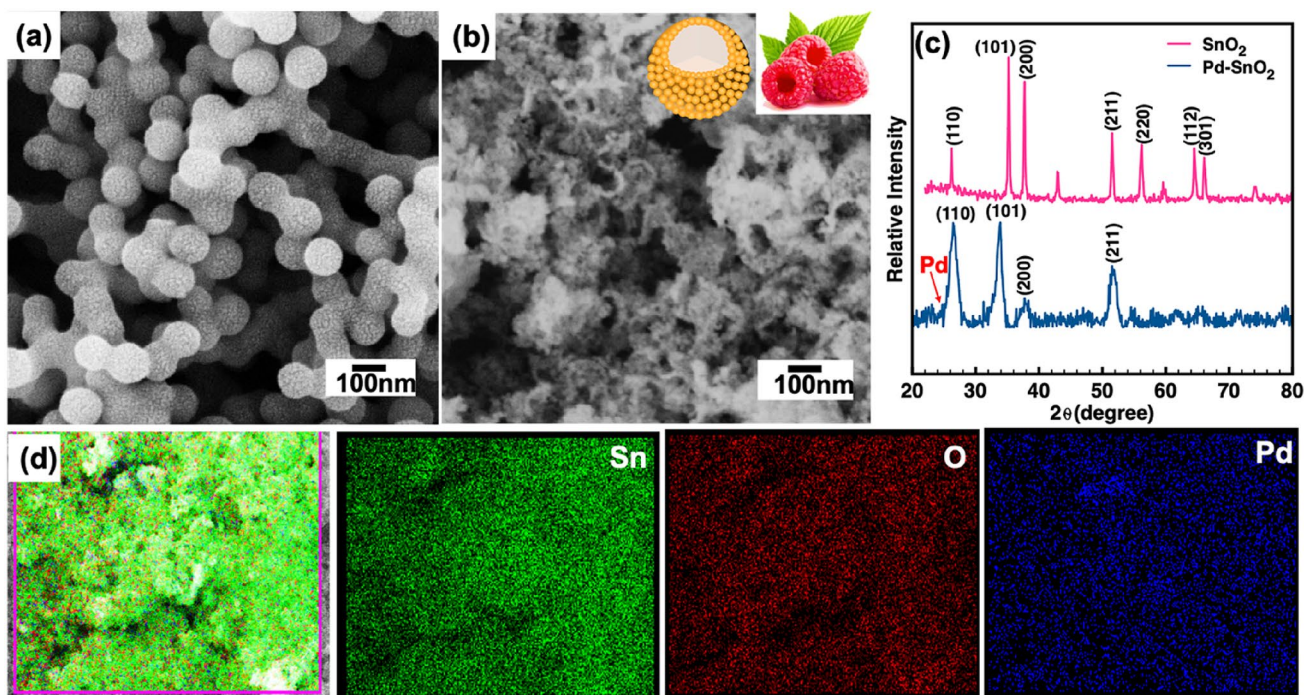

Fig. 2 SEM images of **a** Carbon spheres, **b** Pd-SnO$_2$ powders. **c** XRD patterns for SnO$_2$ and Pd-SnO$_2$ products. **d** EDX analysis of Pd-SnO$_2$

51.9° correspond, respectively, to the (110), (101), (200) and (211) planes of the pure SnO_2. And the strongest two peaks are (101) and (200) in SnO_2. For Pd-SnO_2, however, there is no obvious Pd or PdO_x peaks, which is possibly because of the small amount of Pd. Compared to pure SnO_2, (110) peak of SnO_2 strengthens dramatically while (200) peak almost disappears in Pd-SnO_2. The broaden width and shift of the SnO_2 diffraction peaks with Pd additive could be explained in two aspects: (1) the crystallite size of SnO_2 became smaller after Pd addition; (2) the poor crystallinity of SnO_2 due to strong chemical interactions with Pd additive [23]. The additive Pd phase will be analyzed using XPS in the following. In addition, the EDX analysis for Pd-SnO_2 demonstrates coexistence of Sn, O, and Pd (Fig. 2d). And the distribution of every color confirms these three elements distribute uniformly over the whole outline.

More morphological and crystal structure characterizations for SnO_2 and Pd-SnO_2 were investigated using TEM analysis. The low-resolution TEM images (Fig. 3a, c) further demonstrate the spherical shape and rough surface of SnO_2 and Pd-SnO_2, similar to previous report [5, 6], as well as an obvious void space in the interior confirming the hollow feature. The high-resolution TEM image (Fig. 3b, d) displays SnO_2 is high crystallinity, with the lattice fringe of 3.3, 2.6 and 2.36 Å, respectively, well matched with the (110), (101) and (200) plane of SnO_2 (JCPDS No. 41-1445). The diffraction rings in the SAED patterns (Figure S4) confirm the polycrystalline structure of SnO_2 and Pd-SnO_2 products, which are agree with the XRD patterns (Fig. 2c).
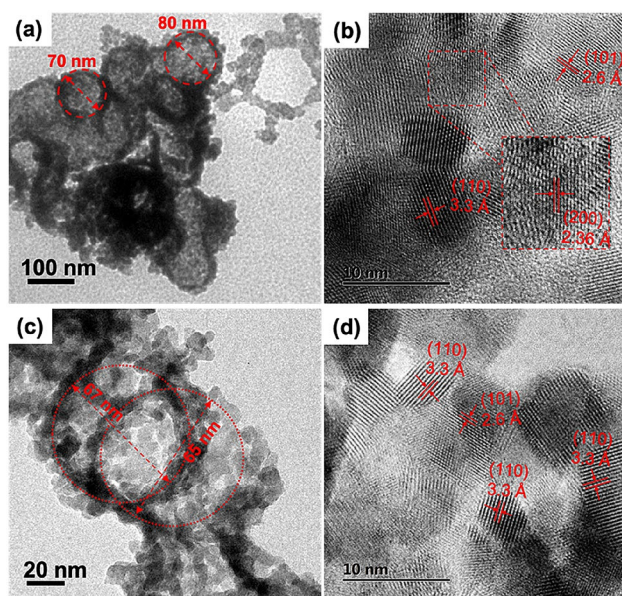
In order to investigate the electronic state and surface chemical composition of elements of SnO_2 and Pd-SnO_2 products, XPS measurement was taken. The binding energy values of Sn 3d, Pd 3d and O 1s, and their atomic percent are listed in Table S1. Obviously, both SnO_2 and Pd-SnO_2 are nonstoichiometric. The survey spectrums of SnO_2 and Pd-SnO_2 are shown in Fig. 4a. For Pd-SnO_2, the relative intensity of Pd 3d binding energy peak is extremely weak because of its low content. In the spectrum of Pd 3d (Fig. 4b), the fitted peaks at 341.87 and 336.59 eV are indexed to Pd^{2+} $3d_{3/2}$ and Pd^{2+} $3d_{5/2}$, respectively, indicating the PdO phase in Pd-SnO_2 due to the oxidation of Pd during calcination process, which is agree with the Ref [24]. Figure 4c demonstrates that the two peaks around at 495.2 and 486.7 eV assigned to Sn^{4+} of Pd-SnO_2 move to low banding energy, compared with those of the pure SnO_2. The Sn 3d peak movement is attributed to the electrons flow from SnO_2 to PdO [15], due to their different Fermi levels (see Sect. 3.3). The obvious deviation further confirms the strong interaction and illustrates heterogeneous formation between SnO_2 and PdO. Figure 4d shows the high-resolution O 1 s core level XPS spectrum and its fitting curve over a small binding energy window for SnO_2 and Pd-SnO_2. It could be resolved into 3 fitted peaks corresponding to O_1, O_2 and O_3. O_1 is ascribed to the lattice oxygen species, having no influence on gas sensing behavior. O_2 and O_3 refers to the oxygen vacancies and chemisorbed oxygen species, respectively, dedicating to the gas sensing properties [25–27].

3.2 Gas sensing performance

For reliable gas sensing measurements, a series of sensors were made from each product. Resistance values of these sensor samples are shown in Fig. S5, indicating resistance of Pd-SnO_2 is much higher than pure SnO_2. Each sensor was measured several times to obtain reliable testing data. According to the I–V curves shown in Fig. S6, nearly linear current vs. voltage behaviors illustrate an Ohmic contact between the sensing materials and sensor electrodes, further demonstrate conductivity of the Pd-SnO_2 is lower than that of pure SnO_2. The higher resistance of Pd-SnO_2 could be explained as follows: according to the XPS analysis, Pd dopant is PdO phase in the Pd-SnO_2 hybrid. The work functions of PdO (5.5 eV) and SnO_2 (4.5 eV) are different. Electrons flow from the conduction band of SnO_2 to PdO, leading to a depletion layer and upward band bending on the surface of SnO_2. Hence, the resistance of Pd-SnO_2 is much higher than that of pure SnO_2.

Prior to investigating the gas sensing performances, selectivity to various gases of the SnO_2 and Pd-SnO_2 sensors was measured. Obviously, the SnO_2 sensor shows excellent selectivity to various VOC gases (ethanol, methanol, acetone, isopropyl alcohol (IPA), formaldehyde), while the Pd-SnO_2

Fig. 3 SnO_2: **a** TEM image and **b** HRTEM image. Pd-SnO_2: **c** TEM image and **d** HRTEM image

Fig. 4 XPS analysis for SnO$_2$ and Pd-SnO$_2$ products: **a** survey spectra, **b** high-resolution spectra of Pd 3d, **c** high-resolution spectra of Sn 3d, and **d** high-resolution spectra of O1s
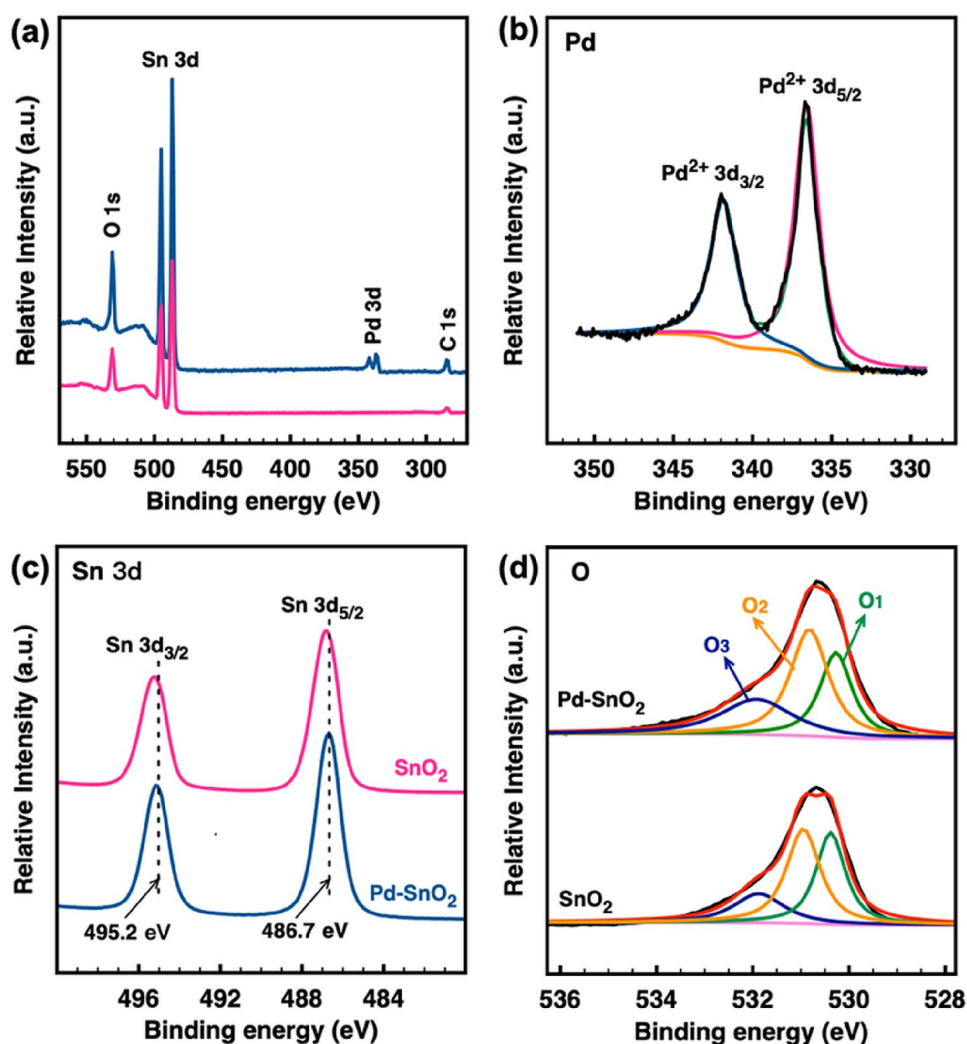
sensor shows great selectivity to NH$_3$ (shown in Fig. 5 a, b). Due to the adsorption/desorption behaviors of oxygen and analyte molecules on the surface of sensing materials are closely related to temperature, the response and response/recovery time of the sensors at different temperatures were studied (Table S2). The response/recovery time of both SnO$_2$ and Pd-SnO$_2$ sensors decrease with the working temperature increasing (Fig. 5c, d). While the response values of the sensors increase at the beginning and then decrease with further increasing in the working temperature, resulting in a peak value at 285 °C for SnO$_2$ sensor to ethanol gas and 240 °C for Pd-SnO$_2$ sensor to ammonia gas. Considering response and recovery performances and power consumption of the devices, 285 °C is taken as the optimum operating temperature. Further tests for both SnO$_2$ and Pd-SnO$_2$ samples are taken at 285 °C under the relative humidity of 40%.

The SnO$_2$ sensor responses to various VOCs (ethanol, methanol, acetone, IPA and formaldehyde) from 1 to 20 ppm at 285 °C are shown in Fig. 6a. Resistance of the SnO$_2$ sensor decreases upon exposure to VOCs, consistent with a n-type semiconductor behavior [28]. Full and rapid recovery of the sensor resistance (e.g., returning back to the baseline), when VOCs is replaced by air, indicates the excellent reversibility of the SnO$_2$ sensor. The response increases with the VOCs gas concentration increasing, while tending to saturate above 20 ppm (Fig. 6b). The typical power-law fitting of acetone response as a function of acetone concentration is shown in Fig. 6b. The similar fitting of the responses vs. concentration for the other VOC gases is shown in Fig. S7.

Figure 6c shows dynamic response-recovery curves of Pd-SnO$_2$ sensor at various NH$_3$ concentrations at 285 °C. The sensor resistance decreases exposed to NH$_3$, indicating the n-type behavior of Pd-SnO$_2$. After the atmosphere returns to air, resistance of the Pd-SnO$_2$ sensor reaches to the initial state in air quickly, exhibiting excellent recovery performance to NH$_3$ exposure. The response to a minimum concentration of 1.5 ppm is very obvious and the power-law fitting can be obtained between the responses and NH$_3$ concentrations, as shown in Fig. 6d. Furthermore, Table 1 summarizes the comparison of NH$_3$ sensing performance
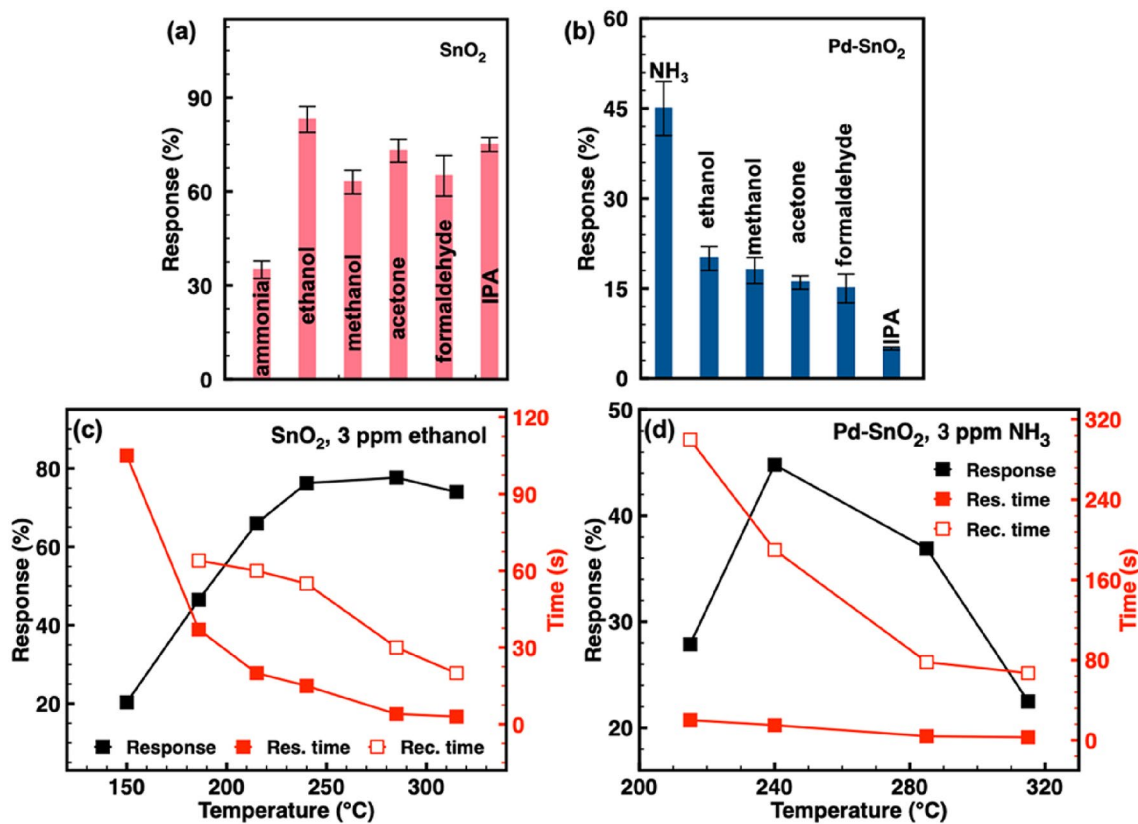
Fig. 5 Selectivity to various gases at 3 ppm at 285 °C: **a** SnO_2 sensor, and **b** Pd-SnO_2 sensor**.** Response values and response/recovery time at different working temperatures (150–315 °C): **c** the SnO_2 sensor to 3 ppm ethanol and **d** the Pd-SnO_2 sensor to 3 ppm NH_3

between our Pd-SnO_2 sensor and previously similar NH_3 sensor based on Pd-functionalized metal oxides. Obviously, the raspberry-like hollow Pd-SnO_2 demonstrates more sensitive to NH_3 gas at low concentrations.

Repeated response/recovery measurements of the SnO_2 sensor to 3 ppm VOCs and that of the Pd-SnO_2 sensor to 3 ppm NH_3 for 8 cycles are shown in Fig. 7a, b, respectively, indicating well repeatable sensing behaviors. Excellent long-term stability of gas sensors is another essential issue for reliable application. Responses of the SnO_2 sensor to 3 ppm ethanol and that of the Pd-SnO_2 sensor to 3 ppm NH_3 were measured over a period of 30 days. As shown in Fig. 7c, the response average variation of around 15% and 8% for SnO_2 and Pd-SnO_2 sensor, respectively. Moreover, repeat response of the Pd-SnO_2 sensor to 1.5 ppm NH_3 under different relative humid conditions (Fig. S8) indicates the stability of the sensor at high working temperature of 285 °C under wide humid conditions (RH% 40–70%).

3.3 Gas sensing mechanism

Response of the SnO_2-based sensor refers to the surface-related redox reaction, depending on the composite and structure of the SnO_2, analyte species and the operating temperature. Among of various nanostructures, the hollow structure here maximizes the gas accessibility of internal surfaces, giving rise to excellent sensing behavior, due to its additional exterior openings and inner voids (Figs. 2b and 3a, c) [6].

The response first step is the surface reaction on SnO_2: the adsorbed oxygen molecules capture electrons from the conduction band of SnO_2, inducing an electron depletion layer on the surface of SnO_2, i.e., a high resistance state. Oxygen chemisorbs on SnO_2 at $T \leq 150$ °C in the molecular form O_2^-, notably, and at higher temperatures it dissociates to atomic O^- [36]. For the present work working at 285 °C, upon exposure to VOCs such as ethanol, the analyte vapor reacts with chemisorbed oxygen species O^- releasing electrons back to sensing material as the following reaction:

$$C_2H_5OH + 6O^-(ad) \rightarrow 2CO_2 + 3H_2O + 6e^- \tag{3}$$
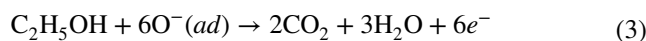
Hence, upon exposed to VOCs, the SnO_2 resistance decreases.

As for the Pd-SnO_2 sensor, there are two sensitization mechanism to explain the improved NH_3 selectivity. For one thing, Pd dopant as PdO phase, observed based on XPS results, introduces a depletion layer on the surface of

Fig. 6 The SnO$_2$ sensor: **a** resistance versus time for various VOCs gas (1–20 ppm) and **b** the corresponding response values with fitting of the typical acetone response as a function of acetone concentration. The Pd-SnO$_2$ sensor: **c** resistance versus time for NH$_3$ gas (1–12 ppm) and **d** the corresponding response values with fitting of the response as a function of NH$_3$ concentration. The error bars represent the standard deviation of response of the 5 exposures to a given target gas concentration
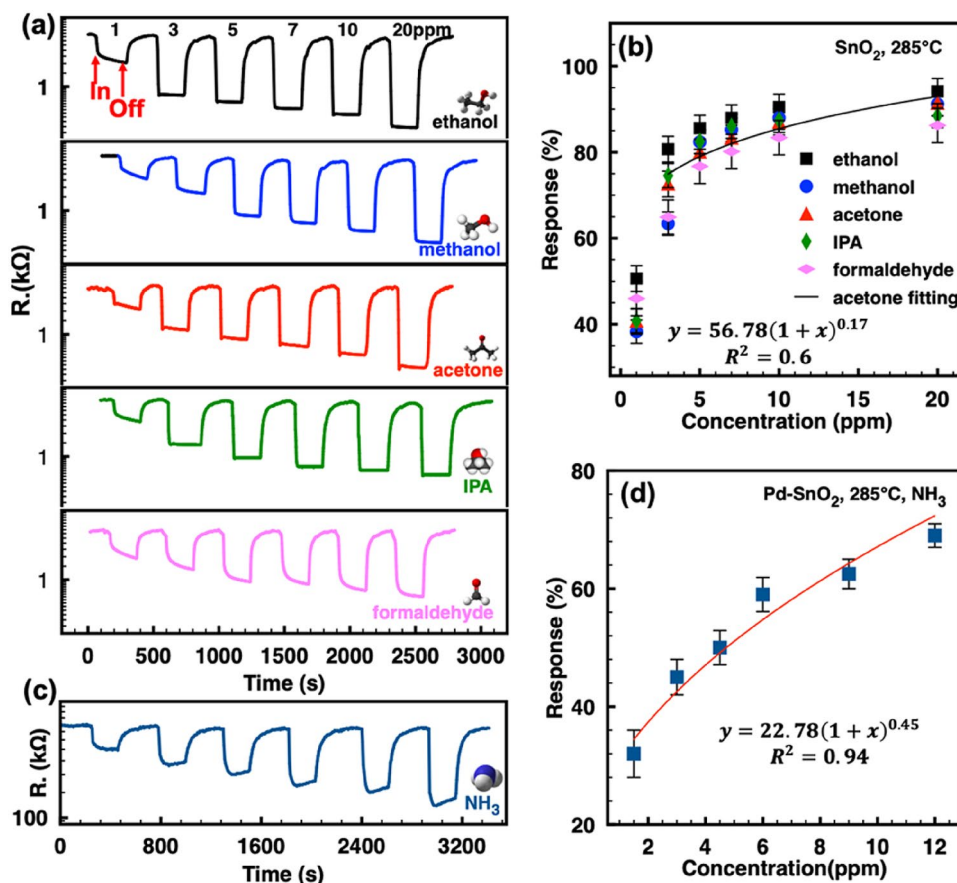

Table 1 Comparison of the NH$_3$ sensing properties of the Pd-SnO$_2$ sensor with previously relative sensors

| Materials	Target gas concentration (ppm)	Operating T (°C)	Response/Recovery time	References
Pd-loaded ZnO NPs	10–40	350	50 s/50 s	[29]
Pd/SnO$_2$/RGO	5–300	RT	7 min/50 min	[30]
Pt/SnO$_2$ thin film	450	230	1 s/59 s	[31]
Bilayer SnO$_2$-WO$_3$ nanofilms	50–1000	300	12 s/58 s	[32]
ppy-SnO$_2$ nanosheets	1–10.7	135	259 s/468 s	[33]
SnS$_2$/SnO$_{2-x}$ nanoflakes	20–400	250	60 s/100 s	[34]
Sn/SnO$_2$/N-doped carbon	5–1000	65	60 s/55 s	[35]
Pd-SnO$_2$	1.5–12	285	4 s/ 80 s	The current work

SnO$_2$ and an upward band bending. It could be explained that PdO traps electrons from the conduction band of SnO$_2$ to equilibrate Fermi level in the hybrid, due to the different work function of PdO (5.5 eV) and SnO$_2$ (4.5 eV). The increased resistance of Pd-SnO$_2$, observed based on I–V behaviors (Figure S3), further probes the initial upward band bending.

For another thing, when the Pd-SnO$_2$ exposed to NH$_3$ vapor, PdO reacts with NH$_3$ and back to Pd^0 as the following reaction [18, 29]:

$$3PdO + 2NH_3 \rightarrow 3Pd^0 + 3H_2O + N_2 \tag{4}$$
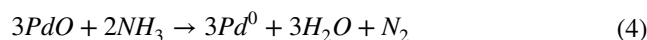
With that, more oxygen chemisorbed on the Pd-SnO$_2$ surface due to the "spillover" effect of Pd^0 as catalyst. It's probably due to that the Pd^0 atoms provide oxygen adsorption sites via available free valences, as well as lower the energy barrier of oxygen adsorption/dissociation [37]. NH$_3$ molecules react with chemisorbed oxygen O^- releasing electrons back to SnO$_2$ and reducing its resistance, according to the following reaction:

Fig. 7 a Repeatability of the SnO$_2$ sensor to 3 ppm VOCs; **b** repeatability of the Pd-SnO$_2$ sensor to 3 ppm NH$_3$; **c** long-term stability of the SnO$_2$ sensor to 3 ppm ethanol and that of the Pd-SnO$_2$ sensor to 3 ppm NH$_3$. The error bars represent the standard deviation of response of the 5 exposures to a given ethanol (or ammonia) gas concentration

$$NH_3 + 4O^-(ad) \rightarrow N_2O + 3H_2O + 4e^- \tag{5}$$

$$NH_3 + 5O^-(ad) \rightarrow 2NO + 3H_2O + 5e^- \tag{6}$$
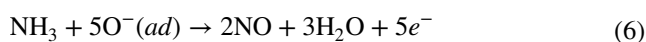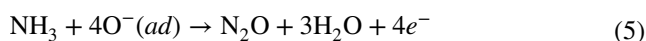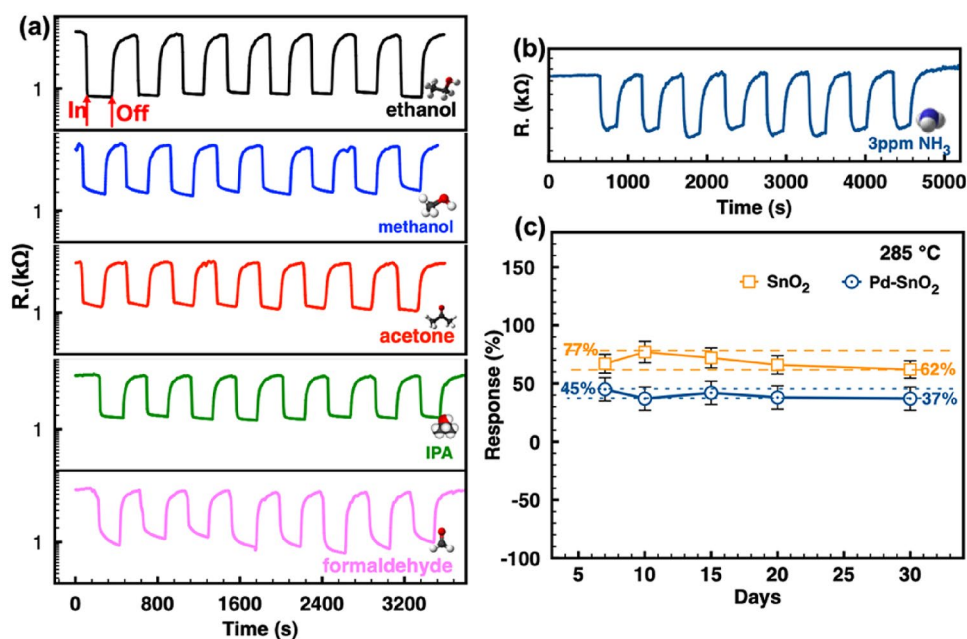
Both the electrical sensitization, upward band bending contribution created by PdO, and the catalytic activation of PdO maximize the NH$_3$ sensing ability of the Pd-SnO$_2$ sensor.

A comparative first-principles calculation was conducted to further clarify the gas sensing mechanism of the SnO$_2$-based materials with different dominant crystal facets. Theorical simulation for gas sensing of Pd-ZnO [38], Pt-SnO$_2$ [39], and CO sensing of Pd-SnO$_2$ [40] have been reported, as well as the NH$_3$ sensing improvement of Pd additive [18, 29, 37]. Moreover, the simulation of VOCs and NH$_3$ adsorption on Pd-SnO$_2$ is quite elusive. Compared the XRD patterns of SnO$_2$ and Pd-SnO$_2$, the main discrepancy is that (110) peak strengthens dramatically while (200) peak tends to disappear after Pd doping. We calculated the adsorption ability of both ethanol (as an example of VOCs) and NH$_3$ on Pd-SnO$_2$ (110) surface, respectively, using Monte Carlo simulation. More details are described minutely in Supporting Information (Fig. S9). The adsorption fields in Fig. 8a, b display the fields of adsorption sites (in white dotted circle), higher density of points showing more likely locations. What's more, the more likely adsorption areas are shown in green and less likely sites appear red. Obviously, compared with ethanol molecule, NH$_3$ is easier to adsorb on the Pd-SnO$_2$ surface. In addition, adsorption energy of NH$_3$ molecule (727 kcal/mol) is much higher than that of ethanol molecule (51 kcal/mol) on Pd-SnO$_2$ (110) facet, further
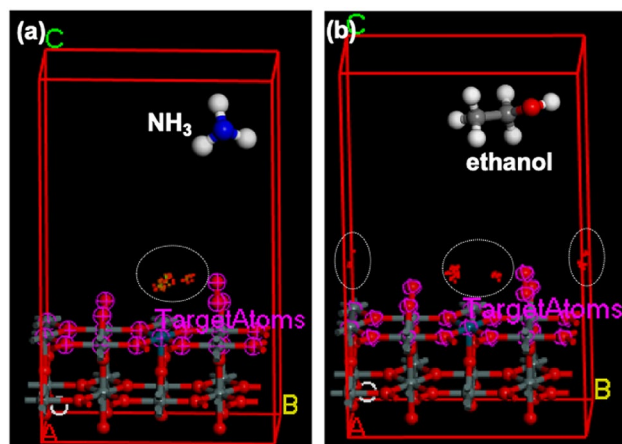

Fig. 8 Adsorption fields: **a** NH$_3$ molecule and **b** ethanol molecule on Pd-SnO$_2$ (110)

verifying the great effect of the Pd additive on the NH$_3$ selectivity of the Pd-SnO$_2$.

4 Conclusions

The raspberry-like hollow SnO$_2$ and Pd-SnO$_2$ nanostructures with different dominated crystal facets were designed and synthesized solvothermally via carbon spheres as templates. Both them possessed additional exterior openings and inner voids, which could contribute to the enhanced gas sensing performances. The pure SnO$_2$ showed great VOCs gas sensing performances, while Pd dopants modulated the NH$_3$ sensing selectivity of the SnO$_2$. The optimum working

temperature for both sensors was found to be 285 °C, with low power, appropriate response, and fast response/recovery behavior. Both the SnO_2 and $Pd-SnO_2$ sensors show great repeatability for 8 response/recovery cycles. But the slight response recession for a long period need to be improved in the future. The corresponding sensing mechanism is explained in terms of morphology, crystallographic facets effect, as well as doping and heterojunctions. The facile approach opens up a prospect for commercialization of the relative micro sensors.

Compliance with ethical standards

References

1. T.T. Lin, X. Lv, Z.N. Hu, A.S. Xu, C.H. Feng, Sensors (2019). https://doi.org/10.3390/s19020233
2. I.P. Liu, C.H. Chang, T.C. Chou, K.W. Lin, Sens. Actuator B **291**, 148 (2019). https://doi.org/10.1016/j.snb.2019.04.046
3. V.B. Raj, A.T. Nimal, Y. Parmar, M.U. Sharma, K. Sreenivas, V. Gupta, Sens. Actuator B **147**, 517 (2010). https://doi.org/10.1016/j.snb.2010.03.079
4. D.D. Nguyen, D.V. Dang, D.C. Nguyen, Adv. Nat. Sci. Nanosci Nanotechnol **6**, 035006 (2015). https://doi.org/10.1088/2043-6262/6/3/035006
5. J. Zhang, S.R. Wang, Y.M. Wang et al., Sens. Actuator B **135**, 610 (2009). https://doi.org/10.1016/j.snb.2008.09.026
6. P.M. Bulemo, H.J. Cho, D.H. Kim, I.D. Kim, ACS Appl Mater Interfaces **10**, 18183 (2018). https://doi.org/10.1021/acsami.8b00901
7. J.Y. Liu, T.S. Wang, B.Q. Wang et al., Sens. Actuator B **245**, 551 (2017). https://doi.org/10.1016/j.snb.2017.01.148
8. B.-Y. Kim, J.S. Cho, J.-W. Yoon et al., Sens. Actuators B **234**, 353 (2016). https://doi.org/10.1016/j.snb.2016.05.002
9. Z. Li, J.X. Yi, Sens. Actuator B **243**, 96 (2017). https://doi.org/10.1016/j.snb.2016.11.136
10. S.L. Bai, W.G. Tong, Y. Tian et al., J. Mater. Sci. **54**, 2025 (2019). https://doi.org/10.1007/s10853-017-1588-2
11. K. Suematsu, H. Uchino, T. Mizukami, K. Watanabe, K. Shimanoe, J. Mater. Sci. **54**, 3135 (2019). https://doi.org/10.1007/s10853-018-3020-y
12. L. Xiao, S.M. Shu, S.T. Liu, Sens. Actuator B **221**, 120 (2015). https://doi.org/10.1016/j.snb.2015.06.099
13. J. Rebholz, K. Grossmann, D. Pham et al., Sensors **16**, 1437 (2016)
14. K. Großmann, K.E. Kovács, D.K. Pham, L. Mädler, N. Barsan, U. Weimar, Sens. Actuators B **158**, 388 (2011)
15. L.P. Yang, X.Y. Zhou, L.F. Song et al., ACS Appl. Nano Mater. **1**, 6327 (2018). https://doi.org/10.1021/acsanm.8b01529
16. F. Gyger, A. Sackmann, M. Hübner et al., Part. Part. Syst. Charact. **31**, 591 (2014). https://doi.org/10.1002/ppsc.201300241
17. J.M. Walker, S.A. Akbar, P.A. Morris, Sens. Actuator B **286**, 624 (2019). https://doi.org/10.1016/j.snb.2019.01.049
18. D. Degler, U. Weimar, N. Barsan, ACS Sens. **4**, 2228 (2019). https://doi.org/10.1021/acssensors.9b00975
19. F. Shao, M.W.G. Hoffmann, J.D. Prades, J.R. Morante, N. Lopez, F. Hernandez-Ramirez, J. Phys. Chem. C **117**, 3520 (2013). https://doi.org/10.1021/jp3085342
20. B. Cho, J. Yoon, M.G. Hahm et al., J. Mater. Chem. C **2**, 5280 (2014). https://doi.org/10.1039/c4tc00510d
21. X. Han, M. Jin, S. Xie, Q. Kuang, L. Zheng, Angew Chem. Int. Ed. Engl. **48**, 9180 (2009)
22. X. Sun, Y. Li, Angew Chem. Int. Ed. Engl. **43**, 597 (2004). https://doi.org/10.1002/anie.200352386
23. T. Takeguchi, O. Takeoh, S. Aoyama, J. Ueda, R. Kikuchi, K. Eguchi, Appl. Catal. A **252**, 205 (2003). https://doi.org/10.1016/S0926-860x(03)00418-6
24. Y. Masayoshi, T. Masaki et al., Sens. Actuators B **136**, 99 (2009)
25. T.S. Wang, S.F. Zhang, Q. Yu et al., Sens. Actuator B **276**, 262 (2018). https://doi.org/10.1016/j.snb.2018.07.020
26. B.Y. Huang, Z.X. Zhang, C.H. Zhao et al., Sens. Actuator B **255**, 2248 (2018). https://doi.org/10.1016/j.snb.2017.09.022
27. L.L. Guo, F. Chen, N. Xie et al., Sens. Actuator B **272**, 185 (2018). https://doi.org/10.1016/j.snb.2018.05.161
28. P. Sun, W. Wang, Y. Liu, Y. Sun, J. Ma, G. Lu, Sens. Actuators B **173**, 52 (2012)
29. G.H. Mhlongo, D.E. Motaung, F.R. Cummings, H.C. Swart, S.S. Ray, Sci. Rep. **9**, 9881 (2019). https://doi.org/10.1038/s41598-019-46247-z
30. P.G. Su, L.Y. Yang, Sens. Actuator B **223**, 202 (2016). https://doi.org/10.1016/j.snb.2015.09.091
31. M. Shahabuddin, A. Sharma, J. Kumar, M. Tomar, A. Umar, V. Gupta, Sens. Actuator B **194**, 410 (2014). https://doi.org/10.1016/j.snb.2013.12.097
32. N. Van Toan, C.M. Hung, N. Van Duy, N.D. Hoa, D.T.T. Le, N. Van Hieu, Mater. Sci. Eng. B **224**, 163 (2017). https://doi.org/10.1016/j.mseb.2017.08.004
33. Y. Li, H.T. Ban, M.J. Yang, Sens. Actuator B **224**, 449 (2016). https://doi.org/10.1016/j.snb.2015.10.078
34. S.G. Leonardi, W. Wlodarski, Y.X. Li, N. Donato, A. Bonavita, G. Neri, J. Alloy Compd. **781**, 440 (2019). https://doi.org/10.1016/j.jallcom.2018.12.110
35. A.M. Al-Enizi, M. Naushad, A.H. Al-Muhtaseb et al., Chem. Eng. J. **345**, 58 (2018). https://doi.org/10.1016/j.cej.2018.03.138
36. A. Rothschild, Y. Komem, Sens. Actuator B **93**, 362 (2003). https://doi.org/10.1016/S0925-4005(03)00212-0
37. D. Koziej, M. Hubner, N. Barsan, U. Weimar, M. Sikora, J.D. Grunwaldt, Phys. Chem. Chem. Phys. **11**, 8620 (2009). https://doi.org/10.1039/b906829e
38. Y.H. Zhang, Y.L. Li, F.L. Gong, K.F. Xie, H.L. Zhang, S.M. Fang, Phys. Chem. Chem. Phys. **21**, 22039 (2019). https://doi.org/10.1039/c9cp04242c
39. D.P. Xue, P.T. Wang, Z.Y. Zhang, Y. Wang, Sens. Actuator B **296**, 126710 (2019). https://doi.org/10.1016/j.snb.2019.126710
40. P. Bechthold, M.E. Pronsato, C. Pistonesi, Appl. Surf. Sci. **347**, 291 (2015). https://doi.org/10.1016/j.apsusc.2015.03.149